PHYSICAL REVIEW A **85**, 013413 (2012)

Molecular above-threshold-ionization angular distributions with attosecond bichromatic intense XUV laser pulses

Kai-Jun Yuan and André D. Bandrauk[*]
Laboratoire de Chimie Théorique, Faculté des Sciences, Université de Sherbrooke, Sherbrooke, Québec, Canada J1K 2R1

(Received 3 October 2011; revised manuscript received 22 December 2011; published 13 January 2012)

Angular distributions of molecular above-threshold ionization (MATI) in bichromatic attosecond extreme ultraviolet (XUV) linear polarization laser pulses have been theoretically investigated. Multiphoton ionization in a prealigned molecular ion $H_2{}^+$ produces clear MATI spectra which show a forward-backward asymmetry in angular and momentum distributions which is critically sensitive to the carrier envelope phase (CEP) ϕ, the time delay $\Delta\tau$ between the two laser pulses, and the photoelectron kinetic energies E_e. The features of the asymmetry in MATI angular distributions are described well by multiphoton perturbative ionization models. Phase differences of continuum electron wave functions can be extracted from the CEP ϕ and time delay $\Delta\tau$ dependent ionization asymmetry ratio created by interfering multiphoton ionization pathways. At large internuclear distances MATI angular distributions exhibit more complex features due to laser-induced electron diffraction where continuum electron wavelengths are less than the internuclear distance.

DOI: 10.1103/PhysRevA.85.013413 PACS number(s): 33.80.Eh, 34.80.Qb, 42.50.Tx

I. INTRODUCTION

Recent developments in the synthesis and characterization of ultrashort laser pulses [1–3] provide the tools necessary for investigating electron dynamics in atoms, molecules, and solids, and bear the promise of electron control in matter [4]. Ultrashort laser pulse technology advances have led to imaging pump-probe techniques such as laser Coulomb explosion imaging (LCEI) [5] for nuclear motion to laser-induced electron diffraction (LIED) [6,7] for coupled electron-nuclear motion. In LIED, the focus is on using near femtosecond (fs) laser-induced electron scattering [8–12] to image molecular structure. Electrons have great potential for probing the time resolved transient structure of molecules, materials, and even biological systems via ultrafast electron diffraction (UED) [13] due to their large scattering cross sections. Furthermore, recent ultrashort laser pulses offer now the possibility of creating coherent electron wave packets (CEWPs) inside molecules on the attosecond (as) time scale and subnanometer size [14,15]. Recently the pump-probe techniques combining an extreme ultraviolet (XUV) attosecond and a femtosecond infrared (IR) pulse have become an important tool in investigations of the characterization of CEWPs. Many methodologies [16–20], such as streaking and interferometry, have been adopted in past research. In particular, by using a train of XUV attosecond pulses and an IR field, Johnsson *et al.* demonstrated that the ion yield in helium can be controlled through pulse time delays, whereas such an effect is absent in argon [21]. They attributed the ionization control in helium to interference between transiently bound (below ionization threshold) electron wave packets which can modulate the probability that an electron is excited out of the atomic ground state. The interferences of atomic electron wave packets from two-path ionizations by XUV and by XUV and IR laser pulses with pulse time delay have been obtained experimentally [22] and simulated numerically [23]. Most recently, based on such pump-probe schemes the high sensitivity to electron-nuclear dynamics in coherent electron-nuclear wave packets has been monitored from molecular high-order harmonic generation (MHOHG) signal intensities generated with few-cycle attosecond laser pulses [24]. Such XUV-pump-XUV-probe experiments at the 1 fs temporal scale have been successfully realized in tracing atomic coherences [25].

The interference effects of coherent electron and nuclear wave packets from one-photon and two-photon processes in the past have been used to control photoelectron angular distributions in atomic and molecular systems [26–28] and the angular distribution of the products in molecular photodissociation [29–31]. The breaking of spatial symmetry in photoelectron angular distributions arising from simultaneous interference photoionization processes was reported in both atomic Rb and molecular NO [26]. Based on a quantum interference between two photoionization processes, a method for measurement of phase differences of continuum electron wave functions was provided in both linearly and elliptically polarized laser fields [28]. A theoretical description of the angular distribution for one- and two-photon transitions was reported including the contribution of interference effects [29]. Such asymmetrical photodissociation and its control can be achieved by symmetry-breaking interference between two multiphoton pathways which produce isoenergy states of different symmetry [31]. However most of these investigations were focused on femtosecond time scales and low photon energy regimes.

In the present work, we focus on the effects of the relative carrier envelope phase (CEP) ϕ and time delay $\Delta\tau$ in an ultrashort (sub-femtosecond and attosecond) two-color XUV laser pulse ionization on the angular distribution of the corresponding photoelectron energy spectra in the symmetric molecular ion $H_2{}^+$. It has been shown previously that with ultrashort intense XUV laser pulses, resulting kinetic energy spectra of protons from Coulomb explosion lead by a simple inversion procedure to reconstruction of the initial nuclear probability distribution [32]. Very recently XUV free-electron

---

[*] andre.bandrauk@usherbrooke.ca

lasers (FEL) have been developed to trace ultrashort nuclear wave packet motions in molecular $D_2{}^+$ and N_2 and to induce isomerization of acetylene cations [33]. Attosecond XUV laser pulses have been used to study interference effects of molecular orbital configurations in LIED [34,35], ultrashort charge transfer processes in ion-atom collisions [36], and effects of the Cooper minimum on photoionization [37] by monitoring the photoelectron momentum and angular distribution in $H_2{}^+$ and H_2 molecules. By two-photon interferometry with identical attosecond XUV pulses the correlation dynamics in coherently excited doubly excited resonances of helium can be extracted in real time [38]. The effects of the CEP of a few-cycle attosecond laser pulse on ionized electron momentum and energy spectra have been well analyzed in atoms [39]. In this paper we present numerical results of angular distribution of photoelectron spectra in a prealigned molecular ion $H_2{}^+$ with two-color XUV linearly polarized attosecond laser pulses by solving numerically the corresponding time-dependent Schrödinger equation (TDSE). Atomic attosecond photoionization processes in the weak field regime have been treated by perturbation theory methods [40]. Here we use a two-dimensional (2D) model, restricting the electron motion in a plane with static nuclei, thus enabling to go beyond perturbation theory and independent of gauge transformations [41]. The two-color XUV ultrashort laser pulses with frequencies $\omega_1 = 0.76$ a.u. (atomic units) $= 20.7$ eV (wavelength $\lambda_1 = 60$ nm) and $\omega_2 = 1.53$ a.u. $= 41.6$ eV ($\lambda_2 = 30$ nm) and duration 1.2 fs are employed to ionize $H_2{}^+$, where $\hbar\omega_1 < I_p$ and $\hbar\omega_2 > I_p$ ($I_p = 1.1$ a.u., ionization potential of $H_2{}^+$ at $R_e = 2.0$ a.u.). Using intensity $I_0 = 10^{14}$ W/cm^2 our simulations generate XUV molecular above-threshold ionization (MATI) spectra. Our similar previous one-dimension (1D) non-Born-Oppenheimer simulations of $H_2{}^+$ under similar conditions [32] showed that nuclear motion is not discernible (measurable) with attosecond pulses due to the large bandwidth and duration shorter than the femtosecond nuclear time scale. We focus therefore on the photoelectron spectra with static nuclei and show that the CEP ϕ and attosecond time delay $\Delta\tau$ dependence of the asymmetry in angular distributions of photoelectron MATI spectra is due to the interference effect of CEWPs from different multiphoton ionization pathways.. For shorter few-cycle XUV laser pulses, the angular distributions show more complex interference characteristic due to the large bandwidth of such pulses [41]. At large internuclear distance configurations effects of LIED or UED occur as well due to the electron wavelengths shorter than the internuclear distance.

The paper is arranged as follows: In Sec. II we briefly describe the computational methods for time-dependent quantum electron wave packet calculations for $H_2{}^+$ from the corresponding TDSE. The results of the photoelectron angular distributions and momentum distributions for different time delay $\Delta\tau$ and CEP ϕ are presented and discussed in Sec. III. Due to the interference effect of coherent continuum electron wave packets from different multiphoton ionization pathways asymmetric photoelectron angular distributions are observed and analyzed based on perturbative models of multiphoton ionization. Finally, we summarize our findings in Sec. IV. (Throughout this paper, a.u., $e = \hbar = m_e = 1$ are used unless otherwise stated.)

II. NUMERICAL METHODS

Considering a static nuclear $H_2{}^+$ molecular ion, the corresponding TDSE is appropriately written with respect to the center of mass of the two protons at positions $\pm R/2$ as

$$i\frac{\partial}{\partial t}\psi(\mathbf{r},t) = \left[-\frac{1}{2}\nabla^2 + V_{en} + V_L(t)\right]\psi(\mathbf{r},t). \tag{1}$$

Here a 2D (planar) model of the laser polarization in the molecular plane is adopted which has been shown to be adequate to describe electron motions in laser fields for two center problems [42]. We use polar coordinates to describe the field-molecule dynamics where the radial and angular variables are easily separated. For the 2D x-aligned $H_2{}^+$ problem in (ρ,θ) polar coordinates, $(x = \rho\cos\theta, y = \rho\sin\theta)$, the corresponding TDSE is

$$\begin{aligned} i\frac{\partial}{\partial t}\psi(\rho,\theta,t) = {} & -\frac{1}{2}\left[\frac{1}{\rho}\frac{\partial}{\partial\rho}\rho\frac{\partial}{\partial\rho} + \frac{1}{\rho^2}\frac{\partial^2}{\partial^2\theta}\right]\psi(\rho,\theta,t) \\ & + [V_{en} + \mathbf{r}\cdot\mathbf{E}(t)]\psi(\rho,\theta,t). \end{aligned} \tag{2}$$

Equation (2) is obtained by using a splitting method in three dimensions which separates the perpendicular z coordinate, thus reducing the problem to 2D [43]. V_{en} is the electron-proton attraction Coulomb potential

$$V_{en} = -\frac{1}{\sqrt{\rho^2 \pm R\rho\cos\theta + R^2/4 + \alpha}}. \tag{3}$$

α is a regularization parameter to remove Coulomb singularities (this corresponds to averaging over the third dimension perpendicular to the plane of the molecule, that is, the z direction). Here we choose $\alpha = 0.35$, allowing the accurate reproduction of the ground, the first excited electronic potential energies, and ionization potential I_p of $H_2{}^+$ [34]. The laser-electron radiative coupling is described by the time-dependent potential $V_L(t)$ in the length gauge for a two-color linear polarization laser pulse,

$$\begin{aligned} \mathbf{E}(t) = \mathbf{E}_1(t) + \mathbf{E}_2(t+\Delta\tau) = {} & \mathbf{e}E_1 f(t)\cos(\omega_1 t + \phi_1) \\ & + \mathbf{e}E_2 f(t+\Delta\tau)\cos[\omega_2(t+\Delta\tau) + \phi_2]. \end{aligned} \tag{4}$$

$\mathbf{e}$ is the laser polarization vector, ω_1 and ω_2 are angular frequencies of the laser pulses $\mathbf{E}_1(t)$ and $\mathbf{E}_2(t)$ corresponding to wavelengths $\lambda_1 = 2\pi c/\omega_1$ and $\lambda_2 = 2\pi c/\omega_2$, and $\Delta\tau$ is the time delay between the two pulses. A smooth pulse envelope $f(t) = \sin^2(\pi t/T)$ with time duration T and maximum amplitude $E_{1,2}$ for intensity $I_{1,2} = cE_{1,2}^2/8\pi$ are adopted in the simulations. The relative CEP between the two-color laser pulses is defined as $\phi = \phi_2 - \phi_1$. For convenience we set $\phi_1 = 0$ and then the relative CEP reduces to $\phi = \phi_2$. We note that the time delay $\Delta\tau$ can be fixed experimentally with zeptosecond (10^{-21} s) accuracy [44].

We solve the 2D TDSE in Eq. (2) by a second-order accurate split-operator method with the time step δt and error δt^3,

$$\begin{aligned} \psi(t+\delta t) = {} & \exp(-iV_I\delta t/2)\exp(-i\,\nabla^2\,\delta t/2) \\ & \times\exp(-i\,\nabla^2\delta t/2)\exp(-iV_I\delta t/2)\psi(t) + O(\delta t^3), \end{aligned} \tag{5}$$

where $V_I = V_{en} + V_L(t)$, combined with a fifth-order finite difference method and Fourier transform technique in the spatial steps $\delta\rho$ and $\delta\theta$ [45]. To circumvent numerical problems with ρ singularities of the Laplacian in polar coordinates (ρ,θ), we adopt a high order Crank-Nicholson method combined with the fifth-order finite difference method to obtain a regularized 2D Laplacian propagator in H_2^+ ensuring unitarity at each time step δt in Eq. (5) [43]. The time step is taken to be $\delta t = 0.01$ a.u. $=$ 0.24 as, the spatial discretization is $\delta\rho = 0.25$ a.u. for a radial grid range $0 \leqslant \rho \leqslant 128$ a.u. and the angle grid step $\delta\theta = 0.025$ rad. To prevent unphysical effects due to the reflection of the wave packet from the boundary, we multiply $\psi(\rho,\theta,t)$ in the radial coordinates at each time step by a "mask function" or absorber with the form

$$g(t) = \begin{cases} 1, & \rho < \rho_a, \\ \cos^{1/8}[\pi(\rho-\rho_a)/2\rho_{\rm abs}], & \rho_a \leqslant \rho \leqslant \rho_{\max}. \end{cases} \tag{6}$$

For all results reported here we set the absorber domain $\rho_a = \rho_{\max} - \rho_{\rm abs} = 104$ a.u. with $\rho_{\rm abs} = 24$ a.u., exceeding well the field induced electron oscillation $\alpha_d = E_0/\omega^2$ of the electron, $\rho_{\max} \gg \alpha_d = 0.1$ a.u. at $I_0 = 10^{14}$ W/cm^2, $\lambda = 60$ nm ($\omega = 0.76$ a.u.).

In order to illustrate the photoelectron angular distribution spectra, the energy dependence of the ionization probabilities is explored based on a Fourier analysis of the associated flux [electron current density $\mathcal{J}(t)$]. The time-dependent electron wave function $\psi(\rho,\theta,t)$ generates the radial flux $\mathcal{J}(t)$ at large distance $\rho_0 = 100$ a.u. before the electron wave packet is absorbed. The electron angular distributions are obtained from

$$\mathcal{J}(\theta,t) = \frac{1}{2i}\left[\psi^*(\rho,\theta,t)\frac{\partial\psi(\rho,\theta,t)}{\partial\rho} - \frac{\partial\psi^*(\rho,\theta,t)}{\partial\rho}\psi(\rho,\theta,t)\right]_{\rho_0}. \tag{7}$$

The total corresponding angular distribution is obtained by integration over time t,

$$\mathcal{J}(\theta) = \int \mathcal{J}(\theta,t)dt, \tag{8}$$

and the energy-resolved angular differential yield (photoelectron spectra) is obtained after a time Fourier transform

$$\mathcal{J}(\theta,E) \sim \int e^{-iEt}\mathcal{J}(\theta,t)dt. \tag{9}$$

The corresponding energy distribution is obtained by integrating over angle θ,

$$\mathcal{J}(E) = \int d\theta \mathcal{J}(\theta,E), \tag{10}$$

where $E = p^2/2$ is the kinetic energy of an ionized electron with wave vector $k = p = 2\pi/\lambda_e$ (in a.u.), p is the momentum of a photoelectron of wavelength λ_e.

An asymmetry ratio as the difference of probability between the positive and negative half of the momentum (angular) distributions at a particular photoelectron kinetic energy E_e can be defined as

$$A(E_e) = \frac{P_+^{E_e} - P_-^{E_e}}{P_+^{E_e} + P_-^{E_e}}, \tag{11}$$

where $P_\pm^{E_e}$ denote the total angular distributions of continuum electron wave packets in forward (+) momentum directions,

$$P_+^{E_e} = \int_{-\pi/2}^{\pi/2} d\theta \mathcal{J}^{E_e}(\theta), \tag{12}$$

or backward ($-$) momentum directions,

$$P_-^{E_e} = \int_{\pi/2}^{3\pi/2} d\theta \mathcal{J}^{E_e}(\theta). \tag{13}$$

The angular distribution $\mathcal{J}^{E_e}(\theta)$ at E_e is obtained by integrating over energy,

$$\mathcal{J}^{E_e}(\theta) = \int_{E_e-\omega/2}^{E_e+\omega/2} dE \mathcal{J}(\theta,E). \tag{14}$$

III. RESULTS AND DISCUSSIONS

In the present work we investigate photoionization processes of a prealigned single electron molecular ion $H_2{}^+$ ionized by an intense ultrashort bichromatic XUV laser pulse with sub-femtosecond and attosecond duration. The two laser wavelengths are set at $\lambda_1 = 60$ nm and $\lambda_2 = 30$ nm, corresponding to angular frequencies $\omega_1 = 0.76$ a.u. $=$ 20.7 eV and $\omega_2 = 2\omega_1 = 1.52$ a.u. $=$ 41.6 eV, which are respectively below and above the equilibrium ($R_e = 2$ a.u.) ionization potential $I_p = 1.1$ a.u. of the $H_2{}^+$ $1s\sigma_g$ electronic state. Such a laser pulse can produce photoelectron wave packets with the same kinetic energies by combination of multiply multiphoton transitions and steer them through different pathways in the continuum, thus creating the interference effects of CEWPs in the photoelectron spectra. In the present calculations the laser polarization is parallel to the molecular axis of $H_2{}^+$ which is aligned with the x axis, and the intensities of the two-color laser pulses are also fixed at $I_1 = 2I_2 = 1.0 \times 10^{14}$ W/cm^2 ($E_1 = \sqrt{2}E_2 = 5.34 \times 10^{-2}$ a.u. $=$ 2.65×10^8 V/cm). At the intensity $I_1 = 1.0 \times 10^{14}$ W/cm^2, (3×10^{-3} a.u.), $\omega_1 = 0.76$ a.u., the ponderomotive energy $U_p = I_1/4\omega_1^2 = 1.2 \times 10^{-3}$ a.u., corresponding to a Keldysh parameter $\gamma = \sqrt{I_p/2U_p} = 21.3 \gg 1$ and thus implying a multiphoton regime.

A. MATI spectra with bichromatic XUV laser pulses

We initially consider the case of photoelectron MATI spectra in a multicycle laser pulse with duration $T = 12\tau = 50$ a.u. $=$ 1.2 fs (1 optical cycle, o.c., $\tau = 2\pi/\omega_2 = 100$ as) for each XUV laser pulse, that is, $T = 6$ o.c. for $\lambda_1 = 60$ nm and $T = 12$ o.c. for $\lambda_2 = 30$ nm laser pulses. We have shown previously that in a multicycle one-color laser pulse the CEP has no influence on the symmetry in the photoelectron angular distributions, and the breaking of symmetry requires shorter few-cycle ($\leqslant 3\tau$) pulses [46]. In Figs. 1(a)–1(c) we illustrate the photoelectron energy spectra calculated by Eq. (10) in the two-color XUV laser pulse [Eq. (4)] with fixed CEP $\phi = 0$ for three different time delays $\Delta\tau = 0$, 4τ (400 as), and 8τ (800 as), respectively. The fundamental XUV laser pulse wavelength and CEP are fixed at $\lambda_1 = 60$ nm and $\phi_1 = 0$, which serves as a reference, while the second $\lambda_2 = 30$ nm XUV laser pulse has variable peak time and phase ϕ_2 ($\phi = \phi_2$),

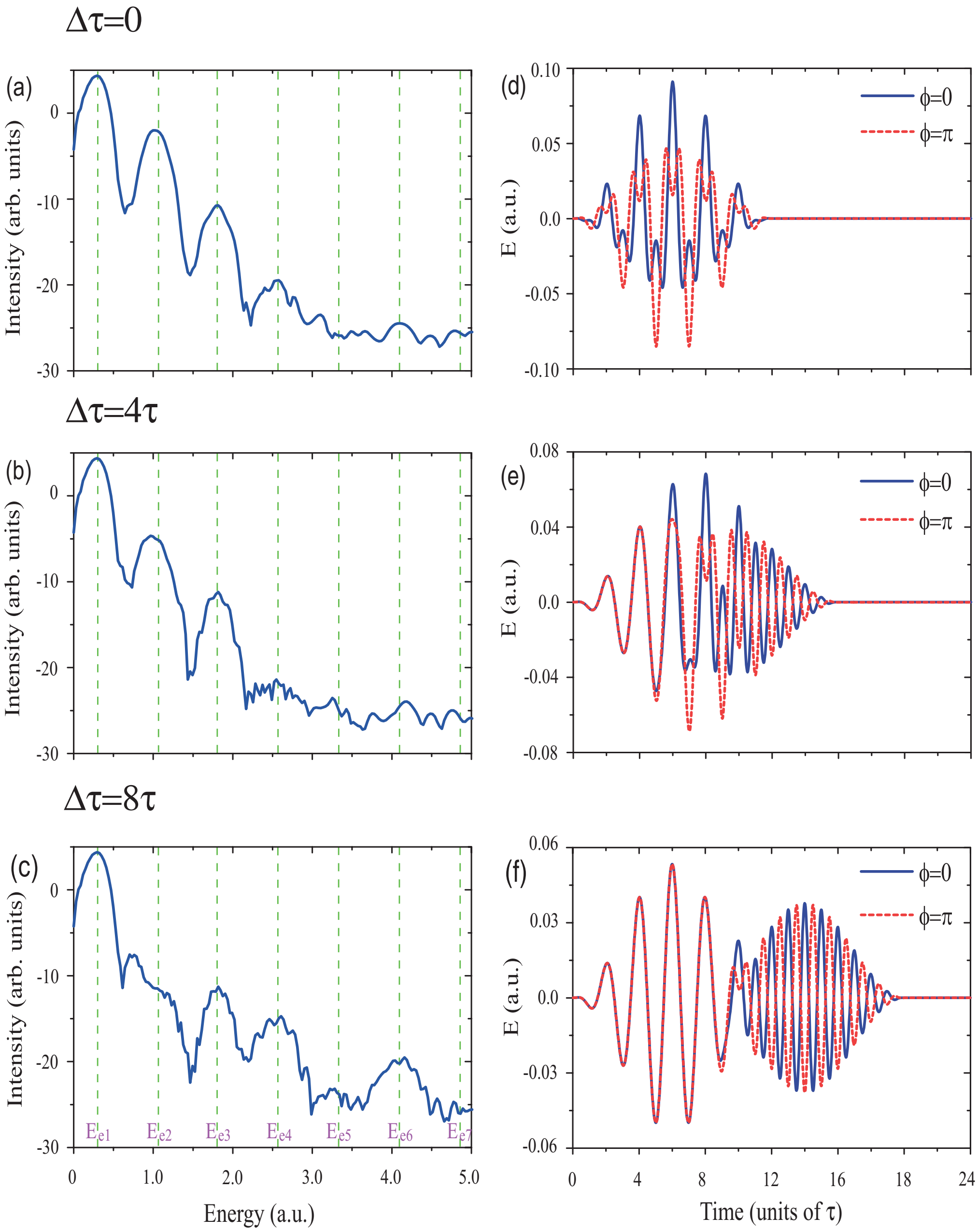

FIG. 1. (Color online) Photoelectron kinetic energy spectra (left column) for prealigned molecular ions $H_2{}^+$ at internuclear distance $R_e = 2$ a.u. in the intense ultrashort bichromatic $\lambda_1 = 60$ nm ($\omega_1 = 0.76$ a.u.) and $\lambda_2 = 30$ nm ($\omega_2 = 1.52$ a.u.) XUV laser pulses (right column) with CEP $\phi = 0$, duration $T = 12\tau = 50$ a.u. $= 1.2$ fs, intensities $I_1 = 2I_2 = 1.0 \times 10^{14}$ W/cm^2, and different time delays [(a), (d)] $\Delta\tau = 0$, [(b), (e)] 4τ (400 as), and [(c), (f)] 8τ (800 as). The classical kinetic energies E_e of MATI peaks are shown as the dashed vertical lines. Signal intensities of the MATI spectra are on a logarithmic scale in arbitrary units.

as shown in Figs. 1(d)–1(f). We note that the vibrational frequency of $H_2{}^+$ is $\omega = 2000$ cm^{-1} with a period of 15 fs, thus confirming that a frozen nuclei calculation is valid for sub-femtosecond and attosecond laser pulses. The laser fields are displayed in Figs. 1(d)–1(f) (blue solid line) for different time delays $\Delta\tau$ and CEPs ϕ.

In Fig. 1 we see that for all cases clear MATI peaks with energy separation $\Delta E = \omega_1 = 0.76$ a.u. have been obtained in the photoelectron spectra. The intensity of the high order MATI peaks varies with time delay $\Delta\tau$. In the XUV laser field of Eq. (4) the MATI spectrum intensity decreases gradually as the photoelectron kinetic energy increases, and high order peaks become very weak. For example, the MATI spectrum in Fig. 1 at photoelectron energy $E_{e4} = 2.58$ a.u. corresponding to $5\omega_1 - I_p$ is more than 8 orders (10^8) weaker than that the first peak $E_{e1} = 0.3$ a.u.. In particular, we note the suppression of the $E_{e5} = 3.34$ a.u. and $E_{e6} = 4.1$ a.u. peaks at $\Delta\tau = 0$, 4τ and the emergence of the E_{e6} peak at $\Delta\tau = 8\tau$. In the following we will mainly focus on the first three low order MATI spectra, E_{e1}, E_{e2}, and E_{e3} peaks. The multiple MATI peaks imply increasing nonperturbative effects which are obtained from the numerical simulations.

B. Asymmetry of MATI angular distributions

Figure 2 shows the 2D momentum (p_x, p_y) distributions of photoelectron spectra for different time delays $\Delta\tau$ and CEPs ϕ of two-color XUV laser pulses. We only illustrate the distributions with low energy photoelectron momentum p ranging from -2 to 2 a.u. ($E_e \leqslant 2$ a.u.) which covers the first three MATI peaks as shown in Fig. 1, where $p_x = p\cos\theta$ and $p_y = p\sin\theta$. In Fig. 2 the results show a time delay $\Delta\tau$ and CEP ϕ sensitive photoionization process. In the momentum distributions (p_x, p_y), the signature of scattering effects appears as nodes or "wings," which are independent of time delay $\Delta\tau$ and CEP ϕ. When the two one-color XUV laser pulses overlap temporally ($\Delta\tau = 0$), the photoelectron momentum distributions display two rings at $p_{e1} = 0.775$ a.u. ($E_{e1} = 0.3$ a.u.), $p_{e2} = 1.456$ a.u. ($E_{e2} = 1.06$ a.u.), and $p_{e3} = 1.908$ a.u. ($E_{e3} = 1.82$ a.u.), that is, the first three MATI peaks separated by one photon energies $\Delta E = 0.76\,\text{a.u.} = \omega_1$, which are asymmetric and mirror image of each other. The asymmetry in positive-negative (forward-backward) momentum distributions strongly depends on the CEP ϕ and photoelectron kinetic energies E_e (p_e). As illustrated in Fig. 2(a) at momentum $p_{e3} = 1.908$ a.u. ($E_{e3} = 1.82$ a.u.), only half "ring" distribution can be observed in the positive or negative momentum plane and a near unidirectional electron flux dominates with maximum asymmetry which depends on the CEP ϕ. Increasing time delay $\Delta\tau$, the photoelectron spectra display a multiring structure gradually, and interference fringes can be observed radially parallel to the laser pulse polarization. With $\Delta\tau = 8\tau$ (800 as) it is almost symmetric with essentially equal electron distributions (flux) in opposite directions for both cases of CEPs $\phi = 0$ and π, that is, with such time delay $\Delta\tau$ the photoelectron angular distributions are mostly independent of the CEP ϕ. Moreover, the momentum distributions exhibit distinct redial interference patterns.

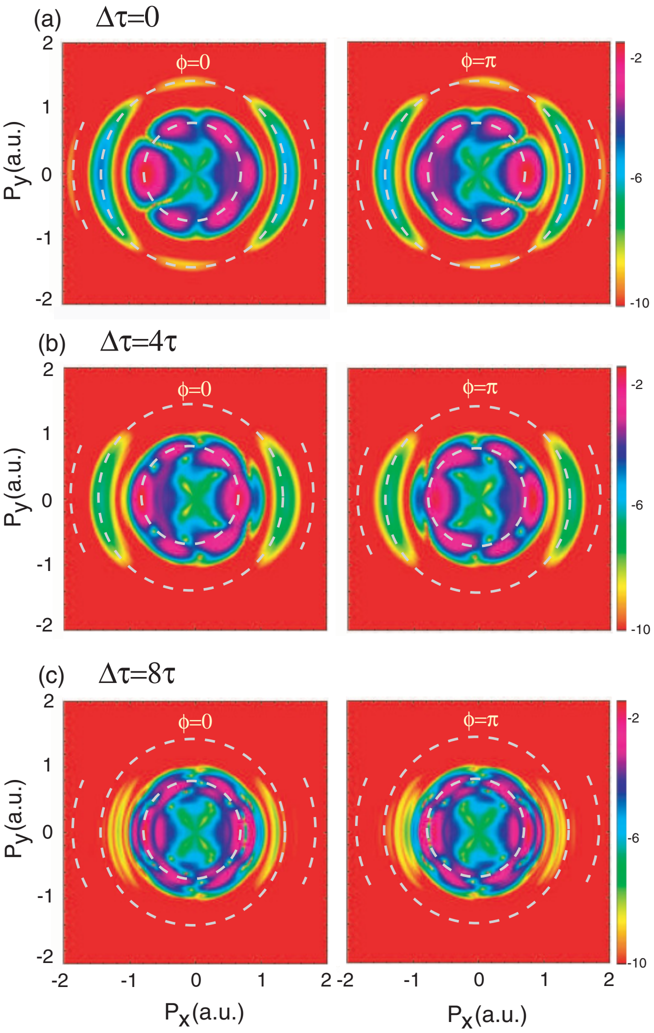

FIG. 2. (Color online) 2D momentum distributions (p_x, p_y) of photoelectron spectra for $H_2{}^+$ at $R_e = 2$ a.u. in the ultrashort bichromatic $\lambda_1 = 60$ nm and $\lambda_2 = 30$ nm XUV laser pulses with duration $T = 12\tau = 1.2$ fs, intensities $I_1 = 2I_2 = 1.0 \times 10^{14}$ W/cm^2, and different CEPs $\phi = 0$ (left column) and π (right column) and time delays (a) $\Delta\tau = 0$, (b) 4τ (400 as), and (c) 8τ (800 as), as shown in Figs. 1(d)–1(f). The classical momenta p_e corresponding to MATI peak energies $E_e = p_e^2/2$ in Fig. 1 are shown as dashed circles with radii $p_{e1} = 0.775$ a.u. ($E_{e1} = 0.3$ a.u.), $p_{e2} = 1.456$ a.u. ($E_{e2} = 1.06$ a.u.), and $p_{e3} = 1.908$ a.u. ($E_{e3} = 1.82$ a.u.).

A perturbative model of multiphoton ionization can be used to describe the CEP ϕ dependent asymmetry of the momentum distribution. In the multiphoton ionization processes, the multipathway CEWPs with anergy E_e will interfere each other in the continuum, leading to the asymmetry. Details are derived in the Appendix. From Eqs. (A10), (A13), and (A18) in the Appendix, we see that for the photoelectron momentum and angular distributions, the CEP dependent asymmetry terms can be simply expressed as

$$\frac{dP_{\text{ion}}^{E_e}}{d\Omega} \propto \cos(\Delta\phi + \Delta\xi) = \cos(\phi + \Delta\xi), \tag{15}$$

where the laser pulse phase difference $\Delta\phi = \phi$. The continuum electron wave function phase difference $\Delta\xi$ is insensitive to the laser pulse CEP ϕ in the perturbative limit. Then the CEP ϕ dependence of angular distributions becomes a function of $\cos\phi$. The relation between asymmetric angular distributions at $\phi = 0$ and π is simply

$$\frac{dP_{\text{ion}}^{E_e}(\phi = 0)}{d\Omega} = -\frac{dP_{\text{ion}}^{E_e}(\phi = \pi)}{d\Omega} \propto \cos(\Delta\xi). \tag{16}$$

From Eq. (16) we see that the angular distributions for CEPs $\phi = 0$ and π do exhibit an exact opposite asymmetry. Therefore as shown in Fig. 2 the momentum distributions of MATI spectra are forward-backward asymmetric in the polarization direction (molecular x axis) and mirror images of each other.

To quantitatively describe the sensitivity of the angular distribution asymmetry to the pulse CEP ϕ, time delay $\Delta\tau$ and photoelectron kinetic energy E_e, in Fig. 3 we show the asymmetry ratio $A(E_e)$ obtained from Eq. (11). In Fig. 3(a) we first show the degree of asymmetry in the angular distributions of photoelectron spectra at particular photoelectron kinetic energies E_e in the two-color XUV laser pulses with varying CEP ϕ from 0 to 2π, where the time delay is fixed at $\Delta\tau = 0$. The photoelectron kinetic energies are respectively $E_{e1} = 0.3$ a.u., $E_{e2} = 1.06$ a.u., and $E_{e3} = 1.82$ a.u. From Fig. 3(a) we see that the asymmetry ratio $A(E_e)$ is a sinusoidal function of the CEP ϕ, in good agreement with the theoretical

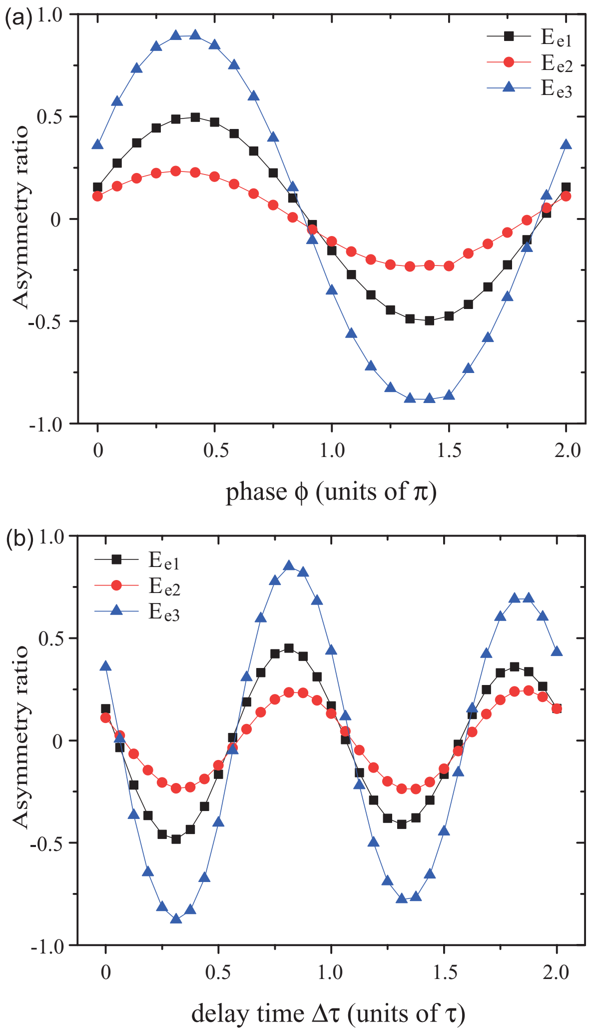

FIG. 3. (Color online) H_2^+ ($R_e = 2$ a.u.) asymmetry ratio $A(E_e)$ [Eq. (11)] of MATI spectra at special photoelectron kinetic energies $E_{e1} = 0.3$ a.u., $E_{e2} = 1.06$ a.u., and $E_{e3} = 1.82$ a.u. as functions of (a) CEP ϕ ($\Delta\tau = 0$) and (b) time delay $\Delta\tau$ ($\phi = 0$) in the ultrashort bichromatic $\lambda_1 = 60$ nm and $\lambda_2 = 30$ nm XUV laser pulse.

predictions $\cos(\phi + \Delta\xi)$ in Eqs. (A10), (A13), and (A18) in the Appendix, thus confirming the multiphoton regime of the processes. The continuum electron wave packet directions after ionization (photoionization angular distributions) are determined by the relative phase of the two laser pulses. Here we emphasize that for the single color multicycle laser pulse no symmetry breaking is appreciably produced, as well as reported in the H atom [46]. On ionization by such bichromatic XUV laser pulses the influence of the interference effect of CWEPs between the two transition pathways results in the CEP ϕ dependent asymmetry in the photoionization angular distributions. This observation also agrees with the results of atomic Rb induced by a bichromatic 280 and 560 nm light [26], where for the one-photon and two-photon ionization processes from the ground $1s\sigma_g$ electronic state, the corresponding angular momenta of the photoelectron are $L = 1$ and $L = 0$ and 2, respectively. In the molecular case, due to nonspherical symmetry, more angular momenta are induced [8,35,47]. The odd and the even electron angular functions will interfere in the continuum, constructively on one side of the electron ionization and destructively on the other side. However for the $\omega_1 + \omega_1 + \omega_1 + \omega_1$ and $\omega_2 + \omega_2$ ionization processes at energies E_{e3}, the corresponding interference effects cannot contribute to the asymmetry in the angular distributions due to the same parity of the continuum electron wave functions [see also Eq. (A14)]. Only the interference between the odd and even parity wave functions in the continuum results in the forward-backward asymmetry in angular distributions. In Eqs. (A10), (A13), and (A18), the phase difference $\Delta\xi$ of continuum electron wave functions is defined by $\Delta\eta - \Delta\phi$. As shown in Fig. 3(a) the degree of asymmetry $A(E_e)$ reaches extreme values $\sim\pm0.5$ for $E_{e1} = 0.3$ a.u. at the CEPs $\phi = 0.4\pi$ and 1.4π, leading to the maximum CEWP interference, constructive and destructive respectively in forward ($\theta = 0^\circ$) and backward ($\theta = 180^\circ$) directions where the transition amplitude phase differences $\Delta\eta = 0$ or π, whereas for values of $A(E_e) \sim 0$ where no interference occurs and $\Delta\eta = \pm\pi/2$, the corresponding CEP is $\phi = 0.9\pi$. Therefore based on the observations of the asymmetry ratio $A(E_{e1})$ one can measure the phase difference of the continuum electron wave functions for two-pathway ionization $\Delta\xi^{E_{e1}} = \Delta\eta - \phi = 0.4\pi$ at E_{e1}.

At higher electron kinetic energies E_{e2} and E_{e3}, similar ionization processes with the interference effects of CEWPs induce the CEP ϕ dependent asymmetry ratios $A(E_{e2})$ and $A(E_{e3})$ in Fig. 3(a). Comparing with $A(E_{e1})$, the degree of symmetry breaking $A(E_{e2})$ is less pronounced, however, $A(E_{e3})$ shows strong asymmetric characteristics with amplitude 0.9. For the MATI peaks at the photoelectron energy E_{e3}, many multiphoton ionization pathway interferences occur, thus enhancing the asymmetry. We conclude that the interference arising from the creation of multipathway electron wave packets is sensitive to the photoelectron kinetic energy E_e. From Fig. 3(a) we get at $E_{e2} = 1.06$ a.u. and the CEPs $\phi = 0.35\pi$ and 1.35π the extreme values are $A(E_{e2}) = \pm0.23$ and $A(E_{e3}) = \pm0.9$ at $E_{e3} = 1.82$ a.u. and the CEPs $\phi = 0.4\pi$ and 1.4π where $\Delta\eta = 0$ or π. For the case of $A(E_{e2}) = A(E_{e3}) = 0$ without interference effects ($\Delta\eta = \pm\pi/2$), the corresponding CEPs are $\phi = 0.85\pi$ and 0.9π. Then the measured phase difference of the transition amplitudes are respectively $\Delta\xi^{E_{e2}} = 0.35\pi$ for E_{e2}, and $\Delta\xi^{E_{e3}} = 0.4\pi$ for E_{e3}. We note that the phase differences $\Delta\xi$ of the continuum electron wave functions at both energies E_{e1} and E_{e3} are nearly equal.

We next investigate the effects of the time delay $\Delta\tau$ on the asymmetry ratio $A(E_e)$. Figure 3(b) displays the results of the MATI spectra at photoelectron kinetic energies $E_{e1} = 0.3$ a.u., $E_{e2} = 1.06$ a.u., and $E_{e3} = 1.82$ a.u. as a function of time delay $\Delta\tau$ where CEP $\phi = 0$. $A(E_e)$ also varies sinusoidally with the time delay $\Delta\tau$, similarly to Fig. 3(a) where $A(E_e)$ illustrates the sensitivity of the CEP ϕ. Varying the time delay $\Delta\tau$ corresponds to altering the CEP of the total laser pulse in Eq. (4), that is, $\omega_2\Delta\tau = \phi'$ [see also Figs. 1(d)–1(f)]. For example, for the ionization at E_{e1} from Fig. 3(b) we obtain that the vanishing asymmetry ratio $A(E_{e1}) = 0$ occurs at approximately $\Delta\tau \approx 0.05\tau$ and the minimum value $A(E_{e1}) = -0.5$ at $\Delta\tau \approx 0.3\tau$ corresponds to phases $\phi' = 0.1\pi$ and 0.6π. From Fig. 3(a) we have measured the phase difference $\Delta\xi = 0.4\pi$. The total phase differences

$\Delta\eta = \omega_2\Delta\tau + \Delta\xi = \phi' + \Delta\xi = 0.5\pi$ and π, which are in good agreement with the predictions in Eq. (A10) where the corresponding interference terms are $\cos(\Delta\eta) = 0$ and -1. Moreover, comparing Figs. 3(a) and 3(b) we note that the asymmetry ratios $A(E_e)$ have oscillation amplitudes which are clearly different. In the case of the CEP ϕ dependence, strong overlap of the two-color laser pulses ($\Delta\tau = 0$) during the ionization processes results in strong interference effects of the CEWPs from the two pathways, therefore leading to constant amplitude of $A(E_e)$. In Fig. 3(b), on the other hand, the longer the time delay $\Delta\tau$, the decreasing overlap of the two-color laser pulses produces less simultaneous interference amplitudes β in Eqs. (A10) and (A13), that is, the asymmetry ratio $A(E_e)$ decreases. Photoionization products show an overall symmetric angular distributions, as illustrated in Fig. 2(c) for the results of $\Delta\tau = 8\tau$ (800 as). By increasing the time delay $\Delta\tau$ of the two laser pulses, the asymmetry of the angular distributions decreases as shown in Fig. 2. The corresponding momentum distribution shown in Fig. 2 illustrates an interference finger with ring structure parallel to laser pulse polarization (radial interference) which is enhanced gradually. When ionization at $\lambda_1 = 60$ nm laser pulse is separated in time from that at $\lambda_2 = 30$ nm as shown in Fig. 1(f), that is, two distinct ionization routes into the continuum, radial interference patterns thus appear clearly. At time delay $\Delta\tau = 4\tau$ (400 as) in Fig. 1(e) one sees that in Fig. 2(b) both simultaneous interference effects and radial interference fingers appear due to superposition of angular momentum states [49]. The radial interference fingers are enhanced as the time delay $\Delta\tau$ increases, as shown in Fig. 2(c) where for time delay $\Delta\tau = 8\tau$ (800 as) triple rings appear clearly around momentum $p = 0.775$ a.u. ($E_{e1} = 0.3$ a.u.). Similar results of evolutions of the asymmetry ratio $A(E_e)$ with time delay $\Delta\tau$ can also observed at different CEPs ϕ, such as π shown in Fig. 1(e) and 1(f), but with a phase shift ϕ.

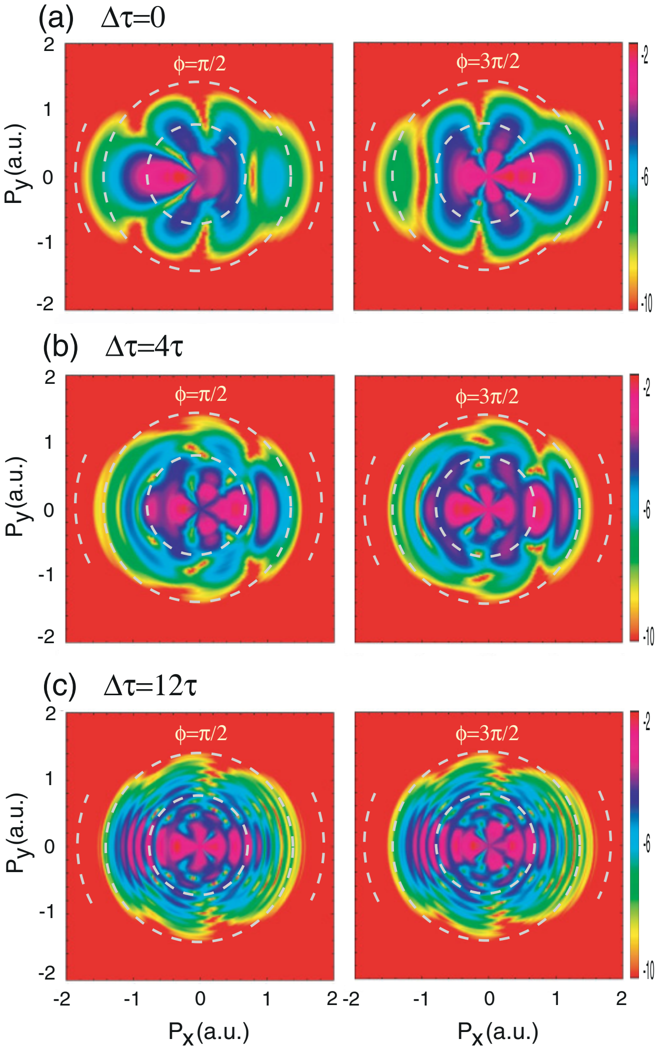

FIG. 4. (Color online) 2D momentum distributions (p_x, p_y) of photoelectron spectra for $H_2{}^+$ at $R = 2$ a.u. in the bichromatic $\lambda_1 = 60$ nm and $\lambda_2 = 30$ nm few-cycle XUV laser pulses with duration $T = 4\tau = 400$ as, intensities $I_1 = 2I_2 = 1.0 \times 10^{14}$ W/cm^2, and different CEPs $\phi = \pi/2$ (left column) and $3\pi/2$ (right column) and time delays (a) $\Delta\tau = 0$, (b) 4τ (400 as), and (c) 12τ (1.2 fs). The classical momenta p_e at MATI peak energies $E_e = p_e^2/2$ (Fig. 1) are shown as dashed circles with radii $p_{e1} = 0.775$ a.u. ($E_{e1} = 0.3$ a.u.), $p_{e2} = 1.456$ a.u. ($E_{e2} = 1.06$ a.u.), and $p_{e3} = 1.908$ a.u. ($E_{e3} = 1.82$ a.u.).

In Fig. 4 we next show the results of the photoelectron momentum (p_x, p_y) distributions for a shorter, few-cycle, attosecond bichromatic intense XUV laser pulse. The laser parameters are the same as those used in Fig. 2 but with fewer cycles $T = 4\tau = 400$ as duration. The pulse CEPs $\phi = \pi/2$ and $3\pi/2$ nearly correspond to the extreme values of $A(E_e)$ in Fig. 3(a). The signature of the CEP ϕ and time delay $\Delta\tau$ dependence on the asymmetry is again clearly observed. For all cases the photoelectron spectra show complicated distributions, and the well-resolved MATI peaks of Fig. 2 disappear. Due to the broad energy width of the attosecond pulse, the ionized electron energy spread increases, simultaneously introducing a spread in electron wave packets. Such an effect appears also in 1D non-Born-Oppenheimer simulations, where all vibrational resolution is lost with sub-femtosecond pulses [32]. Such broad energy and momentum electron wave packets produce additional interference patterns in the photoelectron angular distributions. The scattering nodes in angle as shown in Fig. 2 at $p_{e1} = 0.775$ a.u. are still observed. The Fourier transform of the two-color attosecond XUV pulse with $\Delta\tau = 0$ gives an energy half width $\Delta\varepsilon \approx 0.75$ a.u. For the continuum electron momentum $p = 0.775$ a.u., the momentum width corresponds to $\Delta p = \sqrt{p^2 + 2\Delta\varepsilon} - p = 0.67$ a.u. Analysis of the momentum distributions in Fig. 4 shows the same momentum spread $\Delta p \approx 0.6$ a.u., thus producing wider interference patterns. Increasing the time delay $\Delta\tau$ increases resolution of the spectra, as shown for $\Delta\tau = 12\tau$, where many clear rings appear in Fig. 4(a) due to enhanced radial interference.

C. Effects of LIED at large internuclear distance on MATI spectra

Finally we consider the case of the photoionization for $H_2{}^+$ at a large internuclear distance $R = 10$ a.u. Such large distance geometries are now being considered for attosecond pulse generation due to the high energy MHOHG spectra by electron recombination with neighboring ions [48]. The

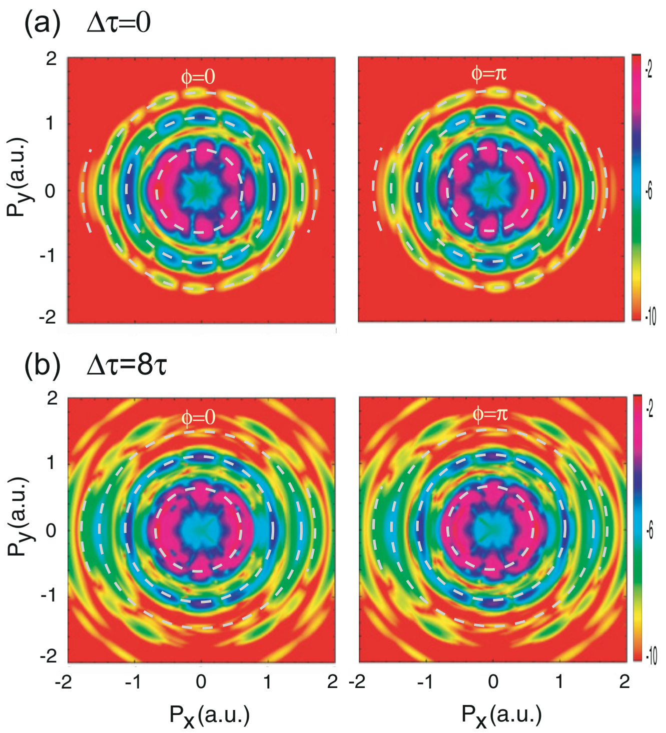

FIG. 5. (Color online) 2D momentum distributions (p_x, p_y) of photoelectron spectra for extended molecular ions $H_2{}^+$ at large internuclear distance $R = 10$ a.u. in the bichromatic $\lambda_1 = 100$ nm ($\omega_1 = 0.456$ a.u.) and $\lambda_2 = 50$ nm ($\omega_2 = 0.91$ a.u.) XUV laser pulses with duration $T = 12\tau = 2.0$ fs, intensities $I_1 = 2I_2 = 1.0 \times 10^{14}$ W/cm^2 and different CEPs $\phi = 0$ (left column) and π (right column) and time delays (a) $\Delta\tau = 0$ and (b) 8τ (1.33 fs). The classical momenta p_e at MATI peak energies $E_e = p_e^2/2$ are shown as dashed circles with radii $p_{e1} = 0.66$ a.u. ($E_{e1} = 0.26$ a.u.), $p_{e2} = 1.16$ a.u. ($E_{e2} = 0.716$ a.u.), $p_{e3} = 1.51$ a.u. ($E_{e3} = 1.172$ a.u.), and $p_{e4} = 1.78$ a.u. ($E_{e4} = 1.628$ a.u.).

dependence of the photoionization angular distributions on the molecular orientation and geometry (internuclear distance R) is in fact a consequence of interference between two single center spherical wave functions [6,34]. The momentum distributions (p_x, p_y) for different time delays $\Delta\tau = 0$ and $8\tau = 1.33$ fs are displayed in Fig. 5. In Fig. 6 we also illustrate the corresponding MATI angular distributions $\mathcal{J}^{E_e}(\theta)$ at three special photoelectron kinetic energies $E_{e1} = 2\omega_1 - I_p$, $E_{e2} = 3\omega_1 - I_p$, and $E_{e3} = 4\omega_1 - I_p$. The same bichromatic intense XUV laser pulse as used in the above simulations is adopted but with longer wavelengthes $\lambda_1 = 100$ nm [$\omega_1 = 0.456$ a.u. $< I_p(R = 10$ a.u.$) = 0.65$ a.u.] and $\lambda_2 = 50$ nm [$\omega_2 = 0.91$ a.u. $> I_p(R = 10$ a.u.$)$] and duration $T = 12\tau = 2.0$ fs. The CEPs in Figs. 5 and 6 are also set at $\phi = 0$ and π. As seen in Figs. 5 and 6, the CEP ϕ and delay time $\Delta\tau$ sensitivity of the forward-backward asymmetry in the momentum distributions can be observed again, the same as the equilibrium photoionization results in Fig. 2. For the large internuclear distance R configurations of the molecular ion $H_2{}^+$, the initial electronic $1s\sigma_g$ state involves a single electron delocalized over two atomic centers since the molecular orbital $\psi_{1s\sigma_g} \sim (1s_a + 1s_b)/\sqrt{2}$. The overall angular distribution is given in [6,34,49] for a $\delta(t)$ excitation pulse for electron momentum $\mathbf{p}$ as

$$\frac{dP_{\text{ion}}^{E_e}}{d\Omega} \propto \mathcal{F}(\Omega)\cos(\mathbf{p}\cdot\mathbf{R}/2). \tag{17}$$

The total angular distribution $\mathcal{F}(\Omega)$ contains now many interference pathways due to the infinite energy width of a $\delta(t)$ pulse. Nevertheless this is modulated by the two center electron phase $\cos(\mathbf{p}\cdot\mathbf{R})/2$ which depends on the internuclear distance R. From Eqs. (A10) and (A13) the angular distribution term $\mathcal{F}(\Omega)$ in Eq. (17) is a function of ϕ $(\Delta\eta)$, therefore we conclude that the asymmetry in forward-backward momentum and angular distributions in Figs. 5 and 6 are mainly due to the constructive and destructive interference effects of the electron wave packets in the continuum which is critically sensitive to the CEPs ϕ and time delay $\Delta\tau$ predicted in Eqs. (A10), (A13), and (A18). As seen in Fig. 6(a) at time delay $\Delta\tau = 0$, the MATI angular distributions show complete asymmetries and mirror images for the CEPs $\phi = 0$ and π at special energies E_e. Increasing time delay $\Delta\tau$ decreases the degree of the asymmetry. At $\Delta\tau = 8\tau$ we see that the asymmetry nearly vanishes and the symmetric angular distributions are obtained for both CEPs $\phi = 0$ and π.

Comparing with Fig. 2, the results illustrated in Figs. 5 and 6 show more complex angular distributions. From Eq. (17) we see that the angular distributions are also functions of the product of internuclear distance and electron momentum: $\mathbf{p}\cdot\mathbf{R}$. At equilibrium in Fig. 2 the electron wavelength $\lambda_e > R_e$ in low energy MATI angular distributions, thus no diffraction occurs. Under the condition of $\lambda_e < R$ the considerable LIED due to electron-proton scattering can be induced. For the photoionization at $R = 10$ a.u. in the bichromatic XUV laser fields, in Fig. 6 the corresponding wavelength of the photoelectron with kinetic energy $E_{e1} = 0.26$ a.u. ($p_1 = 0.72$ a.u.), $E_{e2} = 0.716$ a.u. ($p_2 = 0.1.16$ a.u.), and $E_{e3} = 1.173$ a.u. ($p_3 = 1.51$ a.u.) are, respectively, $\lambda_e = 2\pi/p = 9.5$, 5.4, and 4.2 a.u., less than molecular internuclear distance $R = 10$ a.u., therefore leading to new effects due to electron diffraction. The signature of these diffraction effects appear clearly as "wings" at angles in the corresponding electron angular and momentum distributions in Figs. 5 and 6. For the second MATI peak at photoelectron energy $E_{e2} = 0.715$ a.u. ($p = 1.16$ a.u.), the interference term predicted in [6,34], $\cos(\mathbf{p}\cdot\mathbf{R}/2) = \cos(pR\cos\theta/2)$ has maxima at $\cos\theta = n\pi/6 \simeq 0 \pm 1/2, \pm 1$, that is, $\theta = 0, \pm\pi/3, \pm\pi/2, \pm 2\pi/3$, and π, and for the third MATI peak at $E_{e3} = 1.173$ a.u. ($p_3 = 1.51$ a.u.), $\theta = \pm 35^\circ$, $\pm 65^\circ$, and $\pm\pi/2$. The numerical results in Fig. 6 are consistent with the theoretical predictions. The similar complex LIED and interference patterns in MATI angular distributions for large internuclear distance configurations in $H_2{}^+$ have also been observed in both linearly and circularly polarized $\lambda = 400$ nm laser pulses [50]. In fact increasing the internuclear distance R is similar to the concept of increasing the photon energy to match the internuclear distance. Thus the asymmetry in the angular distributions is dependent on the internuclear distance R as well. Of note is that at delay time $\Delta\tau = 8\tau = 1.33$ fs in Fig. 6(b) no LIED wings appears in the MATI angular distributions at photoelectron kinetic energy E_{e3}. This is mainly results from the weak two-center interference at higher photoelectron energy due to the decrease of the ionization probability and less Coulomb potential effects. At short

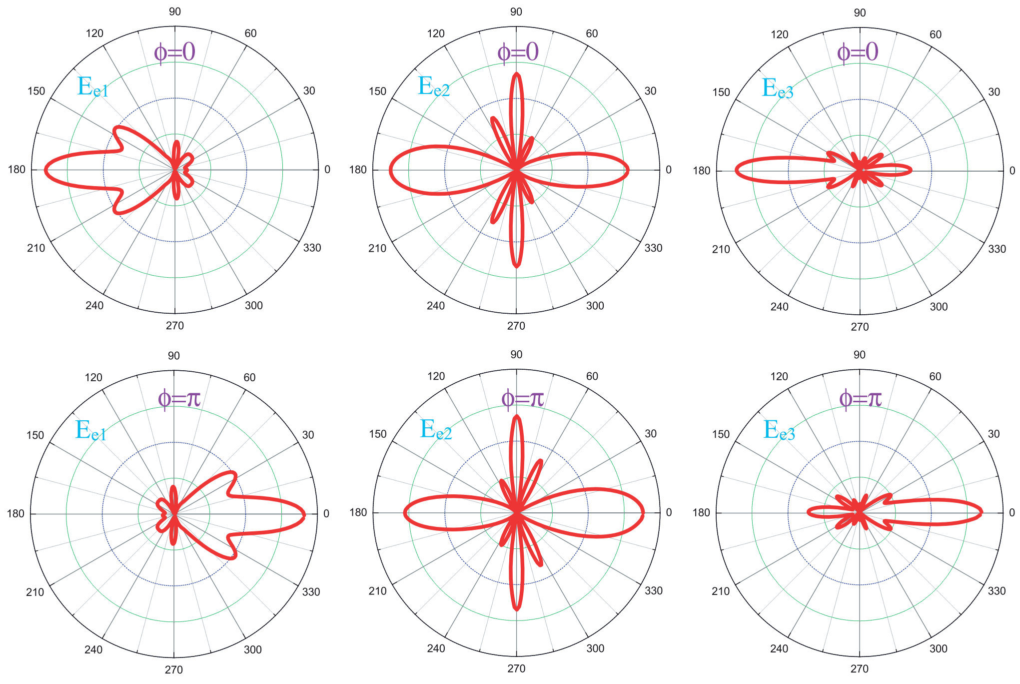
(a) $\Delta\tau=0$

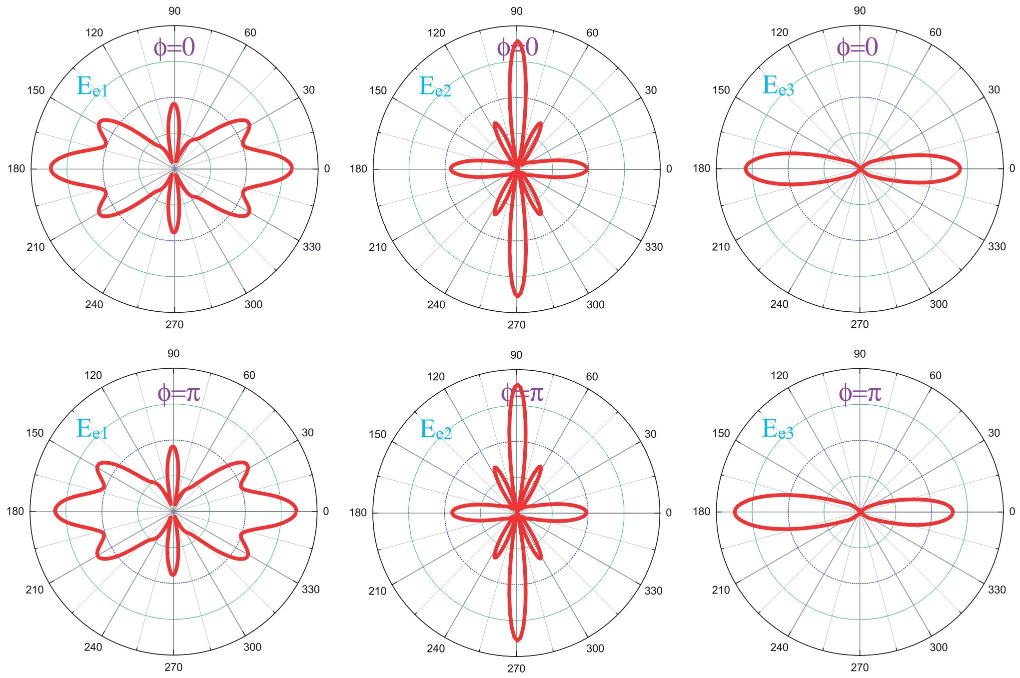
(b) $\Delta\tau=8\tau$

FIG. 6. (Color online) MATI angular distributions $\mathcal{J}^{E_e}(\theta)$ at specific photoelectron kinetic energies (left column) $E_{e1} = 0.26$ a.u., (middle column) $E_{e2} = 0.716$ a.u., and (right column) $E_{e3} = 1.172$ a.u. for molecular ions $H_2{}^+$ at large internuclear distance $R = 10$ a.u. in the bichromatic $\lambda_1 = 100$ nm ($\omega_1 = 0.456$ a.u.) and $\lambda_2 = 50$ nm ($\omega_2 = 0.91$ a.u.) XUV laser pulses with duration $T = 12\tau = 2.0$ fs, intensities $I_1 = 2I_2 = 1.0 \times 10^{14}$ W/cm^2 and different CEPs $\phi = 0$ and π and time delays (a) $\Delta\tau = 0$ and (b) 8τ (1.33 fs), cf. Fig. 5.

time delay $\Delta\tau$, the interference from the multiple pathway ionization shown in Fig. 5 enhances the effects of LIED, thus a clear wing structure is obtained in Fig. 6(a) at E_{e3} for both CEPs $\phi = 0$ and π.

IV. CONCLUSIONS

We have presented MATI angular distributions of a prealigned single electron molecular ion $H_2{}^+$ produced by a combination of ultrashort (few cycles) intense linearly polarized bichromatic XUV laser pulses from numerical solutions of corresponding TDSEs for static nuclei at equilibrium $R_e = 2$ a.u. and large distance $R = 10$ a.u. The ultrashort sub-femtosecond and attosecond pulses frequencies $\omega_2 = 2\omega_1$ are chosen with $\omega_1 < I_p$ and $\omega_2 > I_p$, that is, below and above the ionization potential I_p in order to create interference multiple ionization pathways. The pulse durations are in the attosecond time regime in order to ensure static nuclear configurations as valid models for the patterns of LIED in the ionization. The numerical results show that at intensities $I = 10^{14}$ W/cm^2 and wavelengths $\lambda_1 = 60$ and $\lambda_2 = 30$ nm multiple energy peaks occur in the MATI spectra, thus producing simultaneous LIED spectra at different photoelectron wavelengths λ_e. At equilibrium $\lambda_e > R_e$ negligible diffraction occurs, whereas at $R = 10$ a.u., $\lambda_e < R$, two-center interference patterns are enhanced. The MATI angular distributions at different photoelectron energies E_e exhibit forward-backward asymmetries due to interference effects from multiple ionization pathways illustrated in Fig. 5. These asymmetries are shown to be critically sensitive to the relative CEP ϕ, the time delay $\Delta\tau$ between the two attosecond XUV laser pulses and the MATI photoelectron energies E_e. In general the asymmetric angular distributions are mirror images of each other for the CEPs $\phi = 0$ vs $\phi = \pi$. This behavior is predicted by a perturbative multiple ionization approach resulting in identifiable interference terms which are simple functions of $\cos\theta$, the dipolar interaction, and $\cos\Delta\eta$, where $\Delta\eta = \Delta\phi + \Delta\xi$ with $\Delta\phi$ the phase difference between the electric field amplitudes of each pulse and $\Delta\xi$, the phase difference between the final continuum electron states. An increase in time delay $\Delta\tau$ decreases gradually the degree of the asymmetry in the angular distributions due to decreasing interference between the multiphoton ionization pathways, converging finally to single pulse symmetric angular distributions. Finally, the pulse energy width $\Delta E \sim 1/T$ with T the pulse duration, imposes a limit on MATI energy E and corresponding momentum p resolution. In conclusion, intense attosecond pulses allow for measuring MATI spectra with multiple energy peaks at different static nuclear geometries. The resulting photoelectron spectra exhibit asymmetries in angular distributions for ionization by bichromatic pulses. The asymmetries depend on the relative pulse CEPs but also on the phase difference between final continuum electron wave functions.

ACKNOWLEDGMENTS

The authors thank RQCHP and Compute Canada for access to massively parallel computer clusters and CIPI (Canadian Institute for Photonic Innovations) for financial support of this research in its ultrafast science program.

APPENDIX: PERTURBATIVE MODEL OF MULTIPATHWAY CEWP INTERFERENCE

To understand the sensitivity of the CEP ϕ and time delay $\Delta\tau$ to the asymmetry in the photoionization momentum and angular distributions we adopt a perturbative theoretical model of a multiphoton ionization. Usually for direct one-photon ionization processes by laser pulses, the ionization differential probability can be expressed simply in the dipole form [51]:

$$\frac{dP_{\rm ion}}{d\Omega} \propto \left|\langle\psi_c^{E_e}(\mathbf{r})\middle|T_H|\psi_0(\mathbf{r})\rangle\right|^2 = \left|\langle\psi_c^{E_e}(\mathbf{r})\middle|\mathbf{r}\cdot\mathbf{E}|\psi_0(\mathbf{r})\rangle\right|^2, \tag{A1}$$

where $\psi_c^{E_e}(\mathbf{r})$ is the continuum electron wave function with energy E_e and $\psi_0(\mathbf{r})$ is the initial state. T_H is a transition operator corresponding to the transition from the initial state $|\psi_0\rangle$ to the continuum state $|\psi_c^{E_e}\rangle$. According to the numerical simulation results, here we only consider the case of linearly polarized laser pulses. In a one-color laser pulse, the angular distributions of electrons emitted in one-photon ionization processes have the simple forms respectively $\mathcal{P}(\omega_1) \propto \alpha_0 + \alpha_1\cos^2\theta$, where θ is the angle between the photoelectron momentum $\mathbf{p}$ and orientation of the molecular $\mathbf{R}$ internuclear (laser polarization) axis, and coefficients α_i, $i = 0,1,2,\ldots$, depend on laser pulses and the initial state. Each transition matrix amplitude shows that the CEP ϕ has no influence on the multiphoton ionization angular distributions of the photoelectron spectra.

For a combination of bichromatic laser pulses of frequencies ω_1 and $\omega_2 = 2\omega_1$, the electron can be ionized via multiple pathways to reach the same final energies in the continuum simultaneously. The two-photon $(\omega_1 + \omega_1)$ transition matrix element $\mathcal{A}_{2\omega_1}$ reads in the perturbative dipole approximation as

$$\begin{aligned}
\mathcal{A}_{2\omega_1} &= \langle\psi_c^{E_e}\middle|T_H|\psi_0\rangle \\
&= \int_{\lim\epsilon\to 0} dE_n^e \frac{\langle\psi_c^{E_e}|\mathbf{r}\cdot\mathbf{E}|\psi_n\rangle\langle\psi_n|\mathbf{r}\cdot\mathbf{E}|\psi_0\rangle}{E_0^e - E_n^e + \omega_1 + i\epsilon} \\
&= \mathrm{PP}\int dE_n^e \frac{\langle\psi_c^{E_e}|\mathbf{r}\cdot\mathbf{E}|\psi_n\rangle\langle\psi_n|\mathbf{r}\cdot\mathbf{E}|\psi_0\rangle}{E_0^e - E_n^e + \omega_1} \\
&\quad - i\pi\delta\left(E_0^e - E_n^e + \omega_1\right)\langle\psi_c^{E_e}|\mathbf{r}\cdot\mathbf{E}|\psi_n\rangle\langle\psi_n|\mathbf{r}\cdot\mathbf{E}|\psi_0\rangle \\
&= \mathrm{Re}(\mathcal{A}_{2\omega_1}) + i\,\mathrm{Im}(\mathcal{A}_{2\omega_1}),
\end{aligned} \tag{A2}$$

where the integral sums over all intermediate (virtual) states $|\psi_n\rangle$. Equation (A2) applies to continuum intermediate states $|\psi_n\rangle$ and/or high density Rydberg states [41]. The transition amplitude in Eq. (A2) can thus be written as

$$\begin{aligned}
\mathcal{A}_{2\omega_1} &= \mathcal{R}_{2\omega_1} e^{i\eta_{2\omega_1}}, \\
\mathcal{R}_{2\omega_1} &= \sqrt{[\mathrm{Re}(\mathcal{A}_{2\omega_1})]^2 + [\mathrm{Im}(\mathcal{A}_{2\omega_1})]^2}, \\
\eta_{2\omega_1} &= \tan^{-1}[\mathrm{Im}(\mathcal{A}_{2\omega_1})/\mathrm{Re}(\mathcal{A}_{2\omega_1})],
\end{aligned} \tag{A3}$$

where $\eta_{2\omega_1}$ is the phase of the transition amplitude of the two ω_1 photon ionizations. The total transition matrix element is separated into a nonresonant (virtual) principle part PP integral and a resonant transition $\omega_1 = E_n^e - E_0^e$, where E_0^e and E_n^e is the energies of the initial and intermediate electronic states. For continuum energies or dense states such as Rydberg states, the PP integral becomes negligible due to cancellation from fluctuations of the denominators $E_0^e - E_n^e + \omega_1 > 0$ and $E_0^e - E_n^e + \omega_1 < 0$ in Eq. (A2), that is,

$$\mathrm{PP}\int_{-\infty}^{\infty} dE_n^e \frac{\langle\psi_c^{E_e}|\mathbf{r}\cdot\mathbf{E}|\psi_n\rangle\langle\psi_n|\mathbf{r}\cdot\mathbf{E}|\psi_0\rangle}{E_0^e - E_n^e + \omega_1} = 0. \tag{A4}$$

The nonresonant (virtual) processes in Eq. (A4) occur on a time scale $\tau_{\text{nr}} = 1/|E_0^e - E_n^e + \omega_1|$. In this limit can one assume that the total transition element depends on the resonant process, that is, the imaginary fact of the transition amplitude in Eq. (A2),

$$\mathcal{A}_{2\omega_1} \propto \langle \psi_c^{E_e} |\mathbf{r}\cdot\mathbf{E}|\psi_n\rangle\langle\psi_n|\mathbf{r}\cdot\mathbf{E}|\psi_0\rangle. \tag{A5}$$

In polar coordinates the parallel dipole interaction simply takes the form $\mathbf{r}\cdot\mathbf{E} = rE(\mathbf{r}_0\cdot\mathbf{e}) = rE\cos\theta$, where $\mathbf{r}_0$ is the unit position vector, and then the radial and angular variables in the transition matrix element are easily separated. The transition matrix element $\mathcal{A}_{2\omega_1}$ can then be written as [29]

$$\begin{aligned}\mathcal{A}_{2\omega_1} &\propto T_{2\omega_1} f_{2\omega_1}(\theta) e^{i\xi_{2\omega_1}} E(\omega_1)^2\\ &= T_{2\omega_1} f_{2\omega_1}(\theta) E_0(\omega_1)^2 e^{i\xi_{2\omega_1}+2\phi_{\omega_1}},\end{aligned} \tag{A6}$$

where $\xi_{2\omega_1} = \eta_{2\omega_1}$ is the bound state continuum electron wave function phase and $\phi_{2\omega_1}$ and ϕ_{ω_1} are the pulse CEPs. $T_{2\omega_1}$ and $f_{2\omega_1}(\theta)$ are, respectively, the radial and angular parts of the reduced transition moments. In the case of bound state resonances only, $\text{Im}(\mathcal{A}_{2\omega_1}) = 0$ in Eq. (A2), so the corresponding phase of $\text{Re}(\mathcal{A}_{2\omega_1})$ is the same as the continuum transition amplitude in Eq. (A6) since the final state $|\psi_c\rangle$ is the same.

1. Interference of CEWPs at energy $E_{e1} = 2\omega_1 - I_p$

For the photoelectron angular distributions with energy $E_{e1} = 2\omega_1 - I_p$, that is, simultaneous two-photon ($\omega_1 + \omega_1$) in Eq. (A5) and one-photon ($\omega_2 = 2\omega_1$) ionizations in Eq. (A1), the total transition probability is the square of the two amplitudes with an interference term of the cross products of the two one- and two-photon ionization amplitudes, that is, $dP_{\text{ion}}^{E_{e1}}/d\Omega = \mathcal{P}(2\omega_1) + \mathcal{P}(\omega_2) + \mathcal{P}(2\omega_1,\omega_2)$, where $\mathcal{P}(2\omega_1,\omega_2)$ is the interference term which can be simply written as [28,29]

$$\mathcal{P}(2\omega_1,\omega_2) \propto \mathcal{A}_{2\omega_1}^* \cdot \mathcal{A}_{\omega_2} + \mathcal{A}_{2\omega_1}\cdot\mathcal{A}_{\omega_2}^* \tag{A7}$$

$$= T_{2\omega_1} f_{2\omega_1}(\theta) E_0(\omega_1)^2 E_0(\omega_2)\cos(\Delta\eta), \tag{A8}$$

where $\mathcal{A}_{2\omega_1}$ and $\mathcal{A}_{\omega_2}$ are, respectively, the matrix element of the two- and one-photon absorptions, and the angular factors are obtained in the perturbative limit for linear polarization parallel to the molecular axis,

$$f_{2\omega_1}(\theta) = \langle(\mathbf{r}_0\cdot\mathbf{e})(\mathbf{r}_0\cdot\mathbf{e})(\mathbf{r}_0\cdot\mathbf{e})\rangle = \cos^3\theta. \tag{A9}$$

The two field amplitudes are defined as $E(\omega_2) = E_0(\omega_2)\exp(i\phi_{\omega_2})$ and $E(\omega_1) = E_0(\omega_1)\exp(i\phi_{\omega_1})$. The total phase difference $\Delta\eta$ between the transition amplitudes for the two-pathway ionizations is the sum of difference phases of the laser pulses $\Delta\phi$ and of the continuum electron wave functions $\Delta\xi$, that is, $\Delta\eta = \Delta\phi + \Delta\xi$ with $\Delta\phi = \phi_{\omega_2} - 2\phi_{\omega_1}$ and $\Delta\xi = \xi_{\omega_2} - \xi_{2\omega_1}$, where ξ_{ω_2} and $\xi_{2\omega_1}$ are, respectively, the phases of continuum electron wave functions for direct one ω_2 and two ω_1 photon ionizations. Then the total angular distributions can be finally written as sums of direct and interfering photoionization distributions,

$$\frac{dP_{\text{ion}}^{E_{e1}}}{d\Omega} \propto \alpha_0 + \alpha_1\cos^2\theta + \alpha_2\cos^4\theta + \beta\cos^3\theta\cos(\Delta\eta). \tag{A10}$$

The coefficient β is determined by the intensities of the two laser pulses. We note that Eq. (A10) contains odd order terms in both $\cos\theta$ and $\cos(\Delta\eta) = \cos(\Delta\phi + \Delta\xi)$. The simultaneous interference effect will therefore break the symmetry of the electron flux in forward (positive) and backward (negative) directions and the angular distributions will vary periodically with the phase difference $\Delta\phi$ of the laser pulses. At $\Delta\eta = \pi/2$ there is no interference and at $\Delta\eta = 0$ and π one gets maximum asymmetry as illustrated later.

2. Interference of CEWPs at energy $E_{e2} = 3\omega_1 - I_p$

Photoionization processes can also occur in higher kinetic energy $E_{e2} = 3\omega_1 - I_p$ channels after absorption of three ω_1 photons ($\omega_1 + \omega_1 + \omega_1$), giving a direct transition $\mathcal{P}(3\omega_1)$ with $\alpha_0 + \alpha_1\cos^2\theta + \alpha_2\cos^4\theta + \alpha_3\cos^6\theta$ angular distribution. This is combined with a one ω_1 and one ω_2 photon ($\omega_1 + \omega_2$) transition, giving $\mathcal{P}(\omega_1 + \omega_2) \propto \alpha_0 + \alpha_1\cos^2\theta + \alpha_2\cos^4\theta$ angular distributions. Therefore the simultaneous interference term between these two multiphoton ionization pathways can be written as

$$\begin{aligned}\mathcal{P}(3\omega_1,\omega_1+\omega_2) &\propto \mathcal{A}_{3\omega_1}^*\cdot\mathcal{A}_{\omega_1+\omega_2} + A_{3\omega_1}\cdot\mathcal{A}_{\omega_1+\omega_2}^*\\ &= T_{3\omega_1} f_{3\omega_1}(\theta) E_0(\omega_1)^4 E_0(\omega_2)\cos(\Delta\phi).\end{aligned} \tag{A11}$$

$\mathcal{A}_{3\omega_1}$ and $\mathcal{A}_{\omega_1+\omega_2}$ are transition amplitudes from $\omega_1 + \omega_1 + \omega_1$ and $\omega_1 + \omega_2$ pathway ionizations. The corresponding angular factor is given by

$$f_{3\omega_1}(\theta) = \langle(\mathbf{r}_0\cdot\mathbf{e})^5\rangle = \cos^5\theta. \tag{A12}$$

Then one can express the overall angular distributions

$$\begin{aligned}\frac{dP_{\text{ion}}^{E_{e2}}}{d\Omega} \propto{}& \alpha_0 + \alpha_1\cos^2\theta + \alpha_2\cos^4\theta + \alpha_3\cos^6\theta\\ &+ \beta\cos^5\theta\cos(\Delta\eta),\end{aligned} \tag{A13}$$

where α_i and β are pulse dependent coefficients with transition amplitude phase differences $\Delta\eta = \Delta\phi + \Delta\xi$, $\Delta\phi = \phi_{\omega_2} - 2\phi_{\omega_1}$ and $\Delta\xi = \xi_{\omega_1+\omega_2} - \xi_{3\omega_1}. \xi_{3\omega_1}$ and $\xi_{\omega_1+\omega_2}$ are the phases of the continuum electron wave functions for the $3\omega_1$ and $\omega_1 + \omega_2$ pathways ionizations. The ionization is in fact a three-pathway ionization process. The $\omega_1 + \omega_1 + \omega_1$ transition corresponds to three successive one photon transitions giving rise to a single transition amplitude $\mathcal{A}_{3\omega_1} = \mathcal{R}_{3\omega_1}e^{i\eta_{3\omega_1}}$, whereas the $\omega_1 + \omega_2$ transition corresponds to two amplitudes, $\mathcal{A}'_{\omega_1+\omega_2}$ and $\mathcal{A}'_{\omega_2+\omega_1}$ whose sum is defined as $\mathcal{A}_{\omega_1+\omega_2} = \mathcal{R}_{\omega_1+\omega_2}e^{i\eta_{\omega_1+\omega_2}}$. Again, a phase difference dependent asymmetry in the angular distributions is obtained due to the odd order terms in both $\cos\theta$ and $\cos(\Delta\eta)$ in Eq. (A13).

3. Interference of CEWPs at energy $E_{e3} = 4\omega_1 - I_p$

Similar results for total angular distributions can be obtained for the ionization processes with next higher kinetic energy $E_{e3} = 4\omega_1 - I_p$ via five-pathway transitions after direct absorptions of four ω_1 photons ($\omega_1 + \omega_1 + \omega_1 + \omega_1$), and two 2ω photons ($\omega_2 + \omega_2$), and one 2ω and two ω photons ($\omega_1 + \omega_1 + \omega_2$). For this multipathway ionization, the interference is simply the sum of the contributions from all pathways. We note that in the ionization processes three-pathway interference occurs, that is, the four ω_1 photon ionization with transition $\mathcal{A}_{4\omega_1} = \mathcal{R}_{4\omega_1} e^{i\eta_{4\omega_1}}$, two ω_2 photon ionization with transition $\mathcal{A}_{2\omega_2} = \mathcal{R}_{2\omega_2} e^{i\eta_{2\omega_2}}$, and the three-photon ionization processes $\mathcal{A}_{2\omega_1+\omega_2} = \mathcal{R}_{2\omega_1+\omega_2} e^{i\eta_{2\omega_1+\omega_2}}$ corresponding to three amplitudes $\mathcal{A}'_{2\omega_1+\omega_2}$, $A'_{\omega_1+\omega_2+\omega_1}$, and $A'_{\omega_2+2\omega_1}$ interfere with each other. Then we get respectively $\mathcal{A}_{4\omega_1}$ and $\mathcal{A}_{2\omega_2}$ interference,

$$\mathcal{P}(4\omega_1,2\omega_2) \propto \mathcal{A}^*_{4\omega_1} \cdot \mathcal{A}_{2\omega_2} + A_{4\omega_1} \cdot \mathcal{A}^*_{2\omega_2} = T_{4\omega_1} f_{4\omega_1}(\theta) E(\omega_1)^4 E(\omega_2)^2 \cos(2\Delta\eta_0), \quad \text{(A14)}$$

$\mathcal{A}_{4\omega_1}$ and $\mathcal{A}_{2\omega_1+\omega_2}$ interference,

$$\mathcal{P}(4\omega_1,2\omega_1+\omega_2) \propto \mathcal{A}^*_{4\omega_1} \cdot \mathcal{A}_{2\omega_1+\omega_2} + A_{4\omega_1} \cdot \mathcal{A}^*_{2\omega_1+\omega_2} = T'_{4\omega_1} f'_{4\omega_1}(\theta) E(\omega_1)^6 E(\omega_2) \cos(\Delta\eta_1), \quad \text{(A15)}$$

and $\mathcal{A}_{2\omega_2}$ and $\mathcal{A}_{2\omega_1+\omega_2}$ interference,

$$\mathcal{P}(2\omega_2,2\omega_1+\omega_2) \propto \mathcal{A}^*_{2\omega_2} \cdot \mathcal{A}_{2\omega_1+\omega_2} + A_{2\omega_2} \cdot \mathcal{A}^*_{2\omega_1+\omega_2} = T''_{4\omega_1} f''_{4\omega_1}(\theta) E(\omega_1)^2 E(\omega_2)^2 \cos(\Delta\eta_2), \quad \text{(A16)}$$

where transition amplitude phase differences are $\Delta\eta_0 = \Delta\xi_0/2 + \Delta\phi$, $\Delta\eta_1 = \Delta\xi_1 - \Delta\phi$, and $\Delta\eta_2 = \Delta\xi_2 - \Delta\phi$, and $\Delta\xi_{0,1,2}$ are phase differences of corresponding continuum electron wave functions. The angular parts of the reduced transition matrix elements in Eqs. (A14)–(A16) transform as

$$f_{4\omega_1}(\theta) = \cos^6\theta, \quad f'_{4\omega_1}(\theta) = \cos^7\theta, \quad f''_{4\omega_1}(\theta) = \cos^5\theta. \quad \text{(A17)}$$

The total angular distributions for the E_{e3} MATI peaks at energy $E_{e3} = 4\omega_1 - I_p$ are then

$$\frac{dP^{E_{e3}}_{\text{ion}}}{d\Omega} \propto \alpha_0 + \alpha_1\cos^2\theta + \alpha_2\cos^4\theta + \alpha_3\cos^6\theta + \alpha_4\cos^8\theta + \beta_0\cos^6\theta\cos^2(\Delta\eta_0) + \beta_1\cos^5\theta\cos(\Delta\eta_1) + \beta_2\cos^7\theta\cos(\Delta\eta_2), \quad \text{(A18)}$$

From Eqs. (A14)–(A18) we see that both *odd* and *even* powers of $\cos\theta$ and $\cos(\Delta\eta)$ are obtained in the interference terms, that is, an even number of transition $\cos^6\theta$ term occurs for odd-odd parity interference, whereas the terms $\cos^5(\theta)$ and $\cos^7(\theta)$ correspond to odd-even transition interferences. In Eqs. (A14) and (A17) the term $\cos^6\theta\cos^2(\Delta\eta_0)$ comes from the interference between the four ω_1 and two ω_2 photons ionization processes, which is symmetric in both angle θ and phase difference $\Delta\eta_0$. Thus the interference between $\mathcal{A}_{4\omega_1}$ and $\mathcal{A}_{2\omega_2}$ does not contribute to the asymmetry of the angular distribution. The asymmetry from the $\cos(\Delta\eta)$ [$\cos(\Delta\phi)$] phase term only appears in the high odd multiphoton terms $\cos^5\theta$ and $\cos^7\theta$ via interferences of $\mathcal{A}_{2\omega_1+\omega_2}$ with $\mathcal{A}_{2\omega_2}$ and $\mathcal{A}_{4\omega_1}$ transition amplitudes, respectively.

---

[1] T. Brabec and F. Krausz, Rev. Mod. Phys. **72**, 545 (2000).

[2] F. Krausz and M. Ivanov, Rev. Mod. Phys. **81**, 163 (2009).

[3] Z. Chang and P. Corkum, J. Opt. Soc. Am. B **27**, B9 (2010).

[4] A. D. Bandrauk, M. C. Delfour and C. Le Bris, *Quantum Control: Mathematical and Numerical Challenges* (American Mathematical Society, New York, 2003), Vol. 33.

[5] S. Chelkowski, P. B. Corkum, and A. D. Bandrauk, Phys. Rev. Lett. **82**, 3416 (1999).

[6] T. Zuo, A. D. Bandrauk, and P. B. Corkum, Chem. Phys. Lett. **259**, 313 (1996).

[7] M. Meckel, D. Comtois, D. Zeidler, A. Staudte, D. Pavicic, H. C. Bandulet, H. Pépin, J. C. Kieffer, R. Dörner, D. M. Villeneuve, and P. B. Corkum, Science **320**, 1478 (2008).

[8] M. Peters, T. T. Nguyen-Dang, C. Cornaggia, S. Saugout, E. Charron, A. Keller, and O. Atabek, Phys. Rev. A **83**, 051403 (2011).

[9] P. B. Corkum, Phys. Rev. Lett. **71**, 1994 (1993).

[10] A. D. Bandrauk, S. Chelkowski, and S. Goudreau, J. Mod. Opt. **52**, 411 (2005).

[11] M. Lein, J. P. Marangos, and P. L. Knight, Phys. Rev. A **66**, 051404 (2002).

[12] S. X. Hu and L. A. Collins, Phys. Rev. Lett. **94**, 073004 (2005).

[13] T. Morishita, A. T. Le, Z. Chen, and C. D. Lin, Phys. Rev. Lett. **100**, 013903 (2008).

[14] S. Chelkowski, G. L. Yudin, and A. D. Bandrauk, J. Phys. B **39**, S409 (2006).

[15] H. Niikura, D. M. Villeneuve, and P. B. Corkum, Phys. Rev. Lett. **94**, 083003 (2005).

[16] R. Kienberger, M. Hentsche, M. Uiberacker, C. Spielmann, M. Kitzler, A. Scrinzi, M. Wieland, Th. Westerwalbesloh, U. Kleineberg, U. Heinzmann, M. Drescher, and F. Krausz, Science **297**, 1144 (2002).

[17] A. Palacios, T. N. Rescigno, and C. W. McCurdy, Phys. Rev. Lett. **103**, 253001 (2009).

[18] P. Ranitovic, X. M. Tong, C. W. Hogle, X. Zhou, Y. Liu, N. Toshima, M. M. Murnane, and H. C. Kapteyn, Phys. Rev. Lett. **106**, 193008 (2011).

[19] T. Remetter, P. Johnsson, J. Mauritsson, K. Varjú, Y. Ni, F. Lépine, E. Gustafsson, M. Kling, J. Khan, R. López-Martens, K. J. Schafer, M. J. J. Vrakking, and A. L'Huillier, Nat. Phys. **2**, 627 (2006).

[20] H. C. Shao and A. F. Starace, Phys. Rev. Lett. **105**, 263201 (2010).

[21] P. Johnsson, J. Mauritsson, T. Remetter, A. L'Huillier, and K. J. Schafer, Phys. Rev. Lett. **99**, 233001 (2007).

[22] J. Mauritsson, T. Remetter, M. Swoboda, K. Klünder, A. L'Huillier, K. J. Schafer, O. Ghafur, F. Kelkensberg, W. Siu, P. Johnsson, M. J. J. Vrakking, I. Znakovskaya, T. Uphues, S. Zherebtsov, M. F. Kling, F. Lépine, E. Benedetti, F. Ferrari, G. Sansone, and M. Nisoli, Phys. Rev. Lett. **105**, 053001 (2010).

[23] N. N. Choi, T. F. Jiang, T. Morishita, M. H. Lee, and C. D. Lin, Phys. Rev. A **82**, 013409 (2010).

[24] T. Bredtmann, S. Chelkowski, and A. D. Bandrauk, Phys. Rev. A **84**, 021401(R) (2011).

[25] P. Tzallas, E. Skantzakis, L. A. A. Nikolopoulos, G. D. Tsakiris, and D. Charalambidis, Nat. Phys. **7**, 781 (2011).

[26] Y. Y. Yin, C. Chen, D. S. Elliott, and A. V. Smith, Phys. Rev. Lett. **69**, 2353 (1992); Y. Y. Yin, D. S. Elliott, R. Shehadeh, and E. R. Grant, Chem. Phys. Lett. **241**, 591 (1995).

[27] A. D. Bandrauk and S. Chelkowski, Phys. Rev. Lett. **84**, 3562 (2000).

[28] Z. M. Wang and D. S. Elliott, Phys. Rev. Lett. **87**, 173001 (2001); Phys. Rev. A **62**, 053404 (2000).

[29] H. L. Kim and R. Bersohn, J. Chem. Phys. **107**, 4546 (1997).

[30] M. J. J. Vrakking and S. Stolte, Chem. Phys. Lett. **271**, 209 (1997).

[31] E. E. Aubanel and A. D. Bandrauk, Chem. Phys. Lett. **229**, 169 (1994).

[32] A. D. Bandrauk and S. Chelkowski, Phys. Rev. Lett. **87**, 273004 (2001); S. Chelkowski and A. D. Bandrauk, Appl. Phys. B **74**, S113 (2002).

[33] Y. H. Jiang *et al.*, Phys. Rev. A **81**, 051402 (2010); Phys. Rev. Lett. **105**, 263002 (2010); Phys. Rev. A **82**, 041403 (2010).

[34] K. J. Yuan, H. Z. Lu, and A. D. Bandrauk, Phys. Rev. A **80**, 061403(R) (2009); **83**, 043418 (2011).

[35] D. Pavičić, K. F. Lee, D. M. Rayner, P. B. Corkum, and D. M. Villeneuve, Phys. Rev. Lett. **98**, 243001 (2007).

[36] S. X. Hu, Phys. Rev. A **83**, 041401(R) (2011).

[37] X. Guan, E. B. Secor, K. Bartschat, and B. I. Schneider, Phys. Rev. A **84**, 033420 (2011).

[38] J. Feist, S. Nagele, C. Ticknor, B. I. Schneider, L. A. Collins, and J. Burgdörfer, Phys. Rev. Lett. **107**, 093005 (2011).

[39] L. Y. Peng and A. F. Starace, Phys. Rev. A **76**, 043401 (2007); L. Y. Peng, E. A. Pronin, and A. F. Starace, New J. Phys. **10**, 025030 (2008).

[40] E. A. Pronin, A. F. Starace, M. V. Frolov, and N. L. Manakov, Phys. Rev. A **80**, 063403 (2009); M. V. Frolov, N. L. Manakov, A. A. Silaev, N. V. Vvedenskii, and A. F. Starace, *ibid.* **83**, 021405(R) (2011).

[41] G. L. Kamta and A. D. Bandrauk, Phys. Rev. A **71**, 053407 (2005).

[42] J. Henkel, M. Lein, and V. Engel, Phys. Rev. A **83**, 051401(R) (2011).

[43] A. D. Bandrauk and H. Z. Lu, in *High-Dimensional Partial Differential Equations in Science and Engineering*, edited by A. D. Bandrauk, M. Delfour, and C. LeBris, CRM Lecture Series Vol. 41 (American Mathematical Society, Philadelphia, 2007), pp. 1–15.

[44] T. Bayer, M. Wollenhaupt, C. Sarpe-Tudoran, and T. Baumert, Phys. Rev. Lett. **102**, 023004 (2009).

[45] A. D. Bandrauk and H. Shen, J. Chem. Phys. **99**, 1185 (1993); A. D. Bandrauk and H. Z. Lu, Phys. Rev. A **68**, 043408 (2003).

[46] A. D. Bandrauk, S. Chelkowski, D. J. Diestler, J. Manz, and K. J. Yuan, Int. J. Mass Spectrom. **277**, 189 (2008).

[47] M. Walter and J. Briggs, J. Phys. B **32**, 2487 (1999).

[48] M. Førre, E. Mével, and E. Constant, Phys. Rev. A **83**, 021402 (2011).

[49] S. Selstø, J. F. McCann, M. Førre, J. P. Hansen, and L. B. Madsen, Phys. Rev. A **73**, 033407 (2006).

[50] K. J. Yuan and A. D. Bandrauk, Phys. Rev. A **84**, 013426 (2011).

[51] H. D. Cohen and U. Fano, Phys. Rev. **150**, 30 (1966).